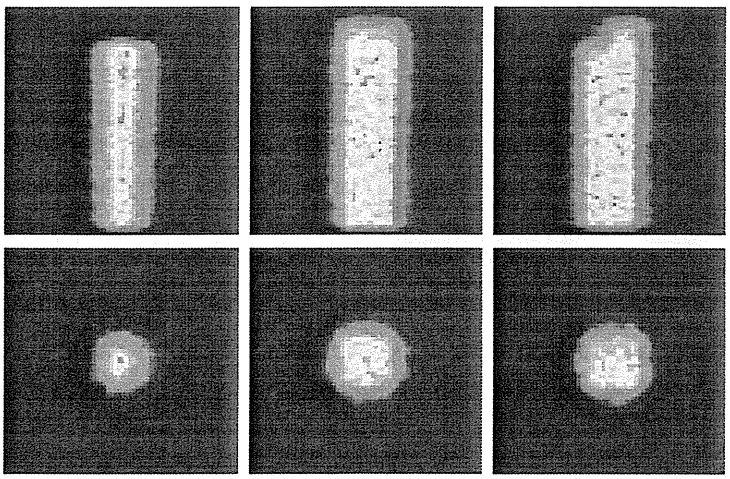

a | b | c

Fig. 5 Two-dimensional distributions of generated positron emitter nuclei in the polyethylene target by irradiation of MONO beams at 179 MeV and 50 mm SOBP beams at 191 MeV, which were measured using the PET apparatus.
The left panels show the distribution of positron emitter nuclei (^{11}C) by irradiation of the MONO beams (a), the middle panels show that by irradiation of the 50 mm SOBP beams (b), and the right panels show that with the range gap created with the patient bolus by irradiation of the 50 mm SOBP beams (c).[6, 7]

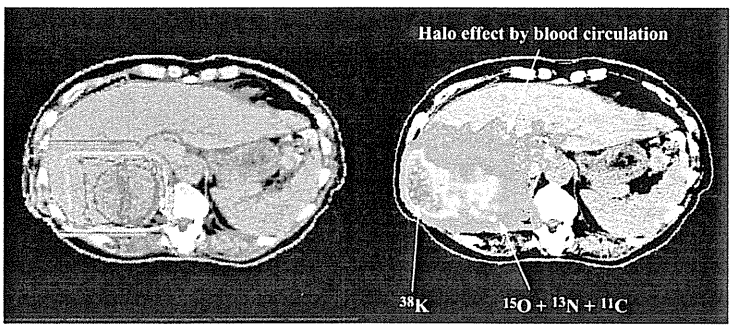

a | b

Fig. 6 Proton dose distribution calculated with the proton treatment planning system (a) and activity distribution measured with the PET apparatus on CT image after proton treatment of tumor in the liver (b).
The proton beam irradiation was performed with gantry angle of 270° and dose of 3.8 GyE.[6]

て，PET 撮影を実施した．

Fig. 5 は，ポリエチレンブロックに陽子線を照射した際，コマーシャルベースの PET 装置によって測定し画像化された結果である．ポリエチレンの組成は水素と炭素であるため，陽子線を照射することで生成されるポジトロン放出核は，炭素核の破砕反応によるものである．その際，陽子線の照射領域の可視化に関係する，生成されたポジトロン放出核は，^{11}C および ^{10}C である．これらのポジトロン放出核を情報因子として陽子線の照射領域が可視化されていることがわかる．179 MeV の MONO，191 MeV の spread-out Bragg peak(SOBP) 50 mm および SOBP 50 mm ビームでレンジにギャップを設け陽子線を照射した．PET 装置による測定は，照射室にてポリエチレンブロックに陽子線を照射後，PET 測定室に移して実施したため，陽子線照射後から PET 装置での測定開始まで，約 5 分の時間が必要であった．その結果，Fig. 5 の画像は半減期が 20 秒と短い ^{10}C はポリエチレンブロック中から消滅しており，半減期が 20 分の ^{11}C のみの分布になっている[6, 7]．

Fig. 6 は肝臓の患者に対して陽子線の照射治療を実施した後に患者へ PET 室に速やかに(約 7 分間で)移動させて撮影した，陽子線治療における患者体内中で照射領域を世界で初めて可視化した結果である[6]．なお，当時は，PET 装置と CT 装置の一体型装置が未開発で，更に画像解析ソフトウェアの充足度も低かったので，CT 画像と PET 画像のフュージョンは自作ソフトウェアで実施したため，線量分布と照射領域可視化領域の幾何学的一致度は低かった．得られた可視化画像から，皮下脂肪と骨の部分では，生成されたポジトロン放出核からの消滅ガンマ線の強度が高いことがわかる．この結果は，陽子線照射後 PET 撮影開始まで移動距離約 40 m，約 7 分間の時間が経過しているため，皮下脂肪では ^{11}C，骨では ^{38}K といった比較的半減期が長いポジトロン放出核のみしか，撮影時には体内に残留していなかったためである．その後，PET/CT 装置の導入に伴って，国立がん研究センター東病院において実施した陽子線治療の内，頭頸部，脳，肝臓，肺，前立腺，および骨軟部の部位について，20 症例を対象に検証した[8]．

6. Prototype beam on-line PET system による照射領域可視化の検証

高い空間位置分解能を有す PET 装置を開発しビームライン上に設置すれば，陽子線治療中に患者体内の何

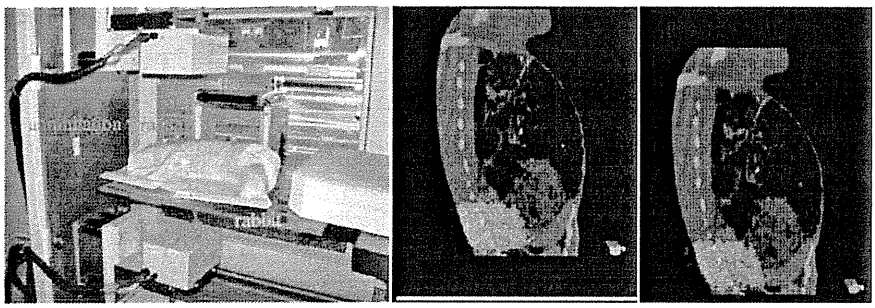

a | b | c

Fig. 7 Proton irradiation to a rabbit and setup of the PT-BOLPs on the proton beamline in the treatment room (a), calculated proton dose distribution (b) and measured PET image using PT-BOLPs (c).[9)]

処に陽子線が照射されているかを観測しながら治療が可能となる．その試験器として，陽子線照射室内のアイソセンタ位置を覆う形で配置される高位置分解能を有すプラナータイプの検出器ヘッドをもつプロトタイプ(prototype)の beam on-line PET system(PT-BOLPs)を構築した[9)]．PT-BOLPs もコマーシャル PET 装置同様，陽子線照射によって患者体内で生成されたポジトロン放出核からの 511 keV の 2 本の消滅ガンマ線を同時計測することで，ポジトロン放出核の位置と activity を決定するための検出システムである．PT-BOLPs の検出器ヘッド部分は，1 個の光電子増倍管に一つが 2×2×20 mm サイズの $Bi_4Ge_3O_{12}$(BGO)結晶を 100 個マウントされた物を 24 ブロック，120.8×186.8 mm の平面上に配置された物である．Fig. 7(a)のように，国立がん研究センター東病院の陽子線治療施設の回転ガントリ治療室に，それを 1 対，上下対向に 500 mm 離して設置した．このシステムは，1.6〜2.1 mm full width at half maximum (FWHM)の高位置分解能をもち，イベントの同時計数率が数 kcps まで不感時間が全く発生しないで，測定およびデータ収集が可能である．

PT-BOLPs によって測定される activity の数は，陽子線照射後の測定開始時間を t_s，測定終了時間を t_e，single 511 keV gamma ray の検出効率を ε，そして PT-BOLPs の全検出立体角を Ω_{sa} として，以下のように表すことができる．

$$N_{\mathrm{BOLPs}}\left(t_i,T_{1/2},t_s,t_e,F,\sigma_{X\to\gamma}\right)$$
$$=N_{act}\left(t_i,T_{1/2},F,\sigma_{X\to\gamma}\right)\cdot 2^{-t_s/T_{1/2}}\cdot\left[1-2^{-(t_e-t_s)/T_{1/2}}\right]\cdot\varepsilon^2\cdot\frac{\Omega_{sa}}{4\cdot\pi}$$
$$=F\left(t_i,E_p\right)\cdot\left[1-\exp\left(-\sigma_{X\to\gamma}\left(A_t,Z_t,E_p\right)\cdot n\cdot\Delta\right)\right]\cdot\left[1+2^{-t_i/T_{1/2}}-\frac{T_{1/2}}{t_i\cdot\ln 2}\cdot\left(1-2^{-t_i/T_{1/2}}\right)\right]$$
$$\times 2^{-t_s/T_{1/2}}\cdot\left[1-2^{-(t_e-t_s)/T_{1/2}}\right]\cdot\varepsilon^2\cdot\frac{\Omega_{sa}}{4\cdot\pi}\qquad\cdots\cdots(1)$$

また，検出器ヘッド間を 500 mm 離した場合での PT-BOLPs の総検出効率 C_{eff} は，以下となる．

$$C_{eff}=\varepsilon^2\cdot\frac{\Omega_{sa}}{4\cdot\pi}\approx 0.86^2\cdot 0.06\approx 0.04\left[\%/100\right]\qquad\cdots\cdots(2)$$

全長 60 cm 程の冷凍されたウサギの形状維持および位置決め用のレーザマーカを付けるために，頭頸部治療で利用している固定シェルをウサギに巻き付け固定させた，CT 撮影，陽子線治療計画，陽子線照射，PT-BOLPs による実測の一連の検証を行った．なお，ウサギの肝臓に対して，照射野サイズは 29×54 mm で背中方向から 4 GyE 照射の治療計画を実施した．Fig. 7 (b)および(c)はウサギへの陽子線照射の線量分布計算結果と PT-BOLPs による測定で得られた PET 画像である[9)]．

陽子線を人体に照射した場合，標的原子核破砕反応によって生成されるポジトロン放出核種は，主な人体構成要素が水素核(^{1}H)，炭素核(^{12}C)，窒素核(^{14}N)および酸素核(^{16}O)であることから，^{15}O(半減期：$T_{1/2}(^{15}\mathrm{O})$=122.2 s)を主成分として，^{14}O($T_{1/2}(^{14}\mathrm{O})$=70.6 s)，^{13}N($T_{1/2}(^{13}\mathrm{N})$=9.971 min)，^{11}C($T_{1/2}(^{11}\mathrm{C})$=20.4 min)であると予想することができる．また，骨に多く含まれるカルシウム核(^{40}Ca)からの生成核種である^{38}K($T_{1/2}(^{38}\mathrm{K})$=7.6 min)も考慮する必要性はあると思われる．しかし，実際には，以下の式で計数率の実験結果：CR(count rate)を短い半減期と長い半減期の 2 成分に分けることによって近似することが可能であった．

$$CR(t)=\sum_{i=^{15}\mathrm{O},^{14}\mathrm{O},^{13}\mathrm{N},^{11}\mathrm{C},\ldots}\left[CR(t)\right]_i=\sum_{j=^{15}\mathrm{O},^{14}\mathrm{O},\ldots}\left[CR(t)\right]_j+\sum_{k=^{13}\mathrm{N},^{11}\mathrm{C},\ldots}\left[CR(t)\right]_k$$
$$\to 1977.9\times\left(\frac{1}{2}\right)^{\frac{t}{110.5}}+219.7\times\left(\frac{1}{2}\right)^{\frac{t}{847.6}}\qquad\cdots\cdots(3)$$

ここで，t は beam stop 後からの測定時間(秒)を表している．

これによって，Fig. 4 に示したような治療期間中の患者の腫瘍の変化を，陽子線照射の度に BOLPs からの

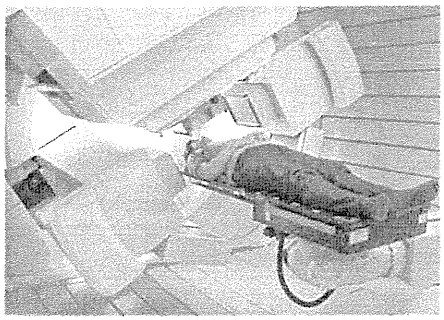

Fig. 8 Setup of the BOLPs-RGp, which is mounted on the rotating gantry port of our proton treatment room.

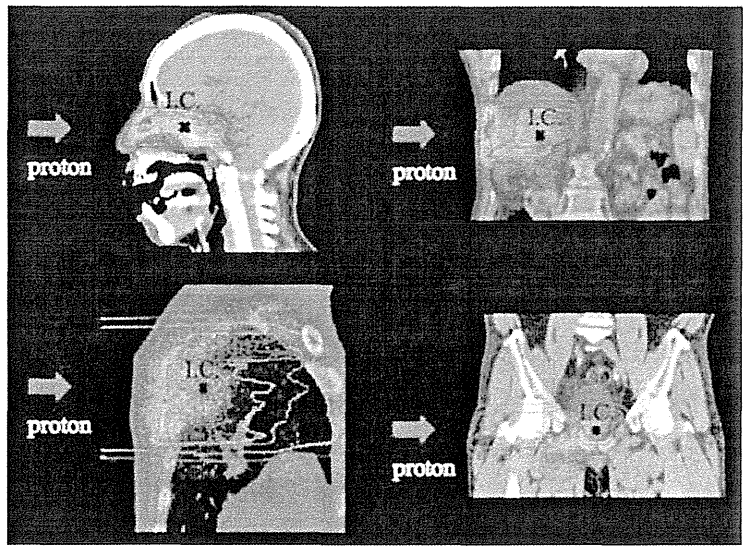

Fig. 9 Proton dose distribution calculated with the proton treatment planning system and activity distribution measured with the BOLPs-RGp on CT image each treatment site.[10)]

a	b
c	d

PET 画像を追跡・把握しながら治療する，現在より高精度の陽子線治療を提供することができる．また，腫瘍状態の変化のみでなく，日々の患者の照射位置に対する位置決め精度や陽子線が作る線量照射野形状の安定性などにも依存した activity 分布形状の変化を見せると思われるので，その変化量は精度として治療計画側へのマージン設定量へフィードバックすることができると考える．更に，高い照射精度が要求されるスキャニング照射法や一回線量を増やした陽子線治療にとって，このシステムの有用性は高いと思われる．

PT-BOLPs の構築およびその研究成果から，臨床における BOLPs の有用性を強く裏付けることができた．回転ガントリに直接設置した臨床用 BOLPs を開発することで，高精度陽子線治療である線量照射誘導陽子線治療が実現可能であることを示唆できた．

7. 臨床用 beam on-line PET system による照射領域可視化の検証

Beam off-line PET system では，標的原子核破砕反応を利用した陽子線照射領域可視化において重要なポジトロン放出核である ^{15}O 核を，可視化の情報因子として利用することができない．その一方で，陽子線照射室内のビームライン上に，高い空間位置分解能を有す beam on-line 型 PET 装置を開発し設置すれば，陽子線治療を行いながら，患者体内の何処に陽子線が照射されているかをリアルタイムで確認できる．そのため，当センターでは，空間分解能が 2 mm のプラナタイプの検出器ヘッドをもつ beam on-line PET system(beam on-line PET system mounted on a rotating gantry port: BOLPs-RGp)を開発した(Fig. 8)[10)]．ガントリの回転に伴って，対向する検出器はアイソセンタを中心に一緒に回転し，検出器面は常に陽子線照射軸を含んでおり，陽子線のレンジ方向を観測できるようになっている．

陽子線治療を行った，頭頸部，前立腺，肝臓，肺および脳の約 150 症例について，各部位に対し，陽子線照射中から照射後 200 秒までの間，BOLPs-RGp で消滅ガンマ線を実測した．日々の陽子線治療において，BOLPs-RGp から得られた照射野可視化画像は 3000 枚以上となった(Fig. 9)[10, 11)]．

BOLPs-RGp の照射領域可視化データによる腫瘍への照射誘導法として，初回の治療で得られた可視化画像をリファレンスとして，それ以降の日々の陽子線治療で得られる可視化画像との時系列変化を観測する手法を考案した(Fig. 10)．可視化画像の相対的形状変化の比較を行うことで，腫瘍とその周囲の重要臓器に対する照射領域を毎回確認し，治療期間中での照射精度を担保できる．それによって，腫瘍へ的確に陽子線が照射されたかを確認しながら，患者へ高精度の陽子線治療を提供することができる．頭頸部，特に副鼻腔の腫瘍は脳幹，視神経などの重要臓器が隣接するため，高い陽子線照射精度が要求される．しかも，副鼻腔部分は骨，空気，そして腫瘍といった密度の違った物質が複雑に入り組んでいるため，線量計算精度が悪化する．そのため，腫瘍が縮小などの変化を起こすことで，

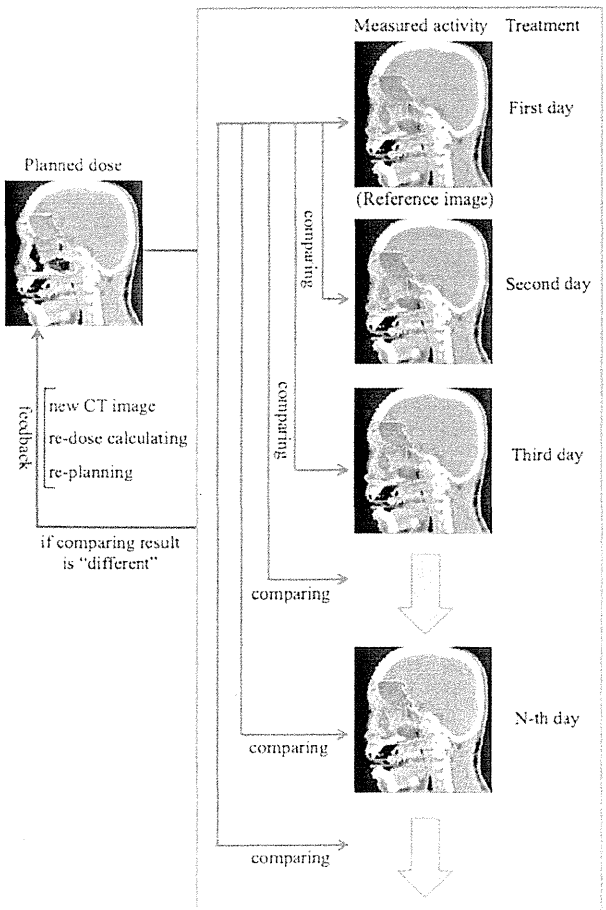

Fig. 10 Flow diagram of the procedure for the clinical use of the BOLPs-RGp.[10]

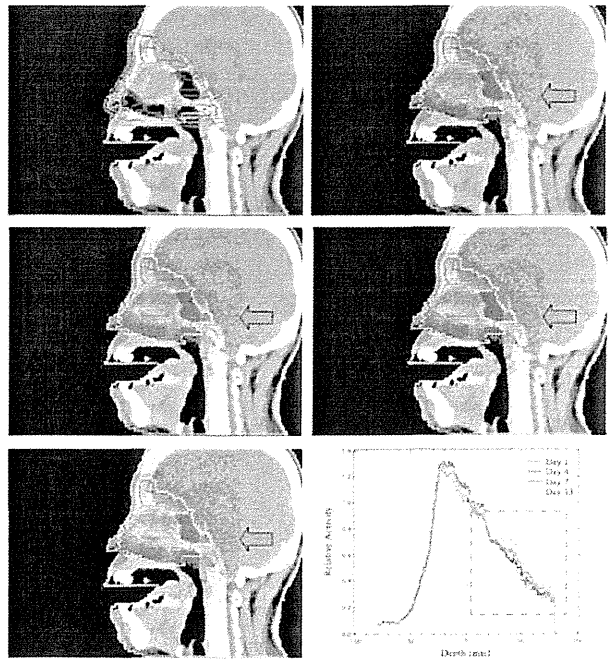

Fig. 11 Proton dose distribution calculated with the proton treatment planning system and activity distribution measured with the BOLPs-RGp in port number 1 irradiation to a head-and-neck patient.

a	b
c	d
e	f

The calculated proton dose distribution (a), the measured activity distribution with BOLPs-RGp at the first treatment (b), the activity at the fourth treatment (the prescribed dose of 7.5 GyE until that day) (c), the activity at the seventh treatment (the prescribed dose of 15 GyE until that day) (d), the activity at the thirteenth treatment (the prescribed dose of 30 GyE until that day) (e) and the depth profile of each measured activity normalized to the iso-center (0-mm depth) of the first activity (f).[10]

腫瘍に対する線量集中性の悪化や重要臓器への線量照射が起こり，腫瘍の制御率の低下と重篤障害を引き起こす可能性が出てくる．

副鼻腔治療のある患者において，1日1門照射で3門の照射，2.5 GyEを26回照射の治療計画で，Fig. 11(a)は治療計画による線量分布の計算結果，(b)，(c)，(d)および(e)は日々の陽子線治療におけるBOLPs-RGpによるactivity分布の実測結果および(f)は日々の実測によって得られたactivity分布を深部方向にプロジェクションしたプロファイルである．治療日数が経過するに連れて，腫瘍の縮小によるactivity分布に変化があることを観測した[10]．その変化量はactivity分布で50%の落ち際で定義したactivityレンジで判断した．65 GyEの線量処方での陽子線治療の計画であったが，35 GyE照射時点でBOLPs-RGpによって日々観測している照射領域可視化画像のactivityレンジがリファレンス(治療初日)のactivityレンジと比較して15 mm近く長くなる，即ち，陽子線のレンジが脳幹側に伸びる傾向が観測され，CTの再撮影と再治療計画を実施した．その再計画によって，腫瘍の体積は184 ccから125 ccに縮小し，最大レンジも水等価深さで20 mm程変化しており，初期の計画では投与されていない重要臓器である脳幹への線量が照射されていたことが判明した[10]．同様に，頭頸部(副鼻腔腫瘍)の陽子線治療においては，全46症例中3症例で治療途中での腫瘍の変化による脳幹への陽子線の誤照射を，観測された照射領域の可視化画像の変化から同定し，速やかに再計画へフィードバックをすることができた．また，壊死した肝臓腫瘍の場合においては，腫瘍内で生成されたポジトロン放出核のwashout効果が優位的に遅いことが観測された[10]．この結果は患者ごとの線量感受性から個別の処方線量を決定できる可能性を示唆している．

8. まとめと今後

入射陽子核と患者体内を構成する原子核との間で起こる標的原子核破砕反応から生成されるポジトロン放出核を利用した陽子線治療の照射領域可視化の研究を，コマーシャルPET装置が医療分野に導入され始めた頃から実施してきた．

BOLPs-RGpを開発し，陽子線治療において実際に陽子線が照射されている領域を治療しているその場で可視化画像として視覚確認できるようになった．また，日々の陽子線治療で取得される照射領域可視化情報から，画像上のactivity分布形状の変化を時系列的に観測することで，陽子線の投与線量に関係した腫瘍形状の変化，または患者の体型変化に伴う線量集中性の精度悪化を観測し，陽子線照射条件を腫瘍形状および患者体型の変化に適応させる高精度陽子線治療を実現させた．更に，陽子線照射によって標的原子核破砕反応で患者体内に生成されたポジトロン放出核が示す血流効果を観測することで，肝腫瘍に関しては，投与線量と血流効果との間に相関があることがわかった．この効果は，患者個別の腫瘍の線量応答や臓器の代謝効率を判断する指標となる可能性を十分に秘めている．

開発したBOLPs-RGpは，陽子線治療の普及装置に装備することが可能なように，現在は陽子線治療装置メーカから国内の医療機器申請中である．その後はUS Food and Drug Administration(FDA)申請も実施予定である．

これまでの研究成果であるBOLPs-RGpの構築や照射領域の可視化情報となる患者体内中での生成ポジトロン放出核の特性を十分把握したことで，標的原子核破砕反応による線量照射誘導陽子線治療を実現することができた．しかし，標的原子核破砕反応による線量照射誘導陽子線治療において，その定義として挙げた3項目の内，三つ目の「腫瘍への投与線量の絶対値を定量的に判断する」に関しては，まだ，多くの研究課題が残っている．生成されるポジトロン放出核のactivity分布から，その強度と陽子線の投与線量の関係を導くには，陽子線照射によるactivity分布計算手法を確立させる必要がある[12, 13]．そのためには，精度として不十分な物理過程を含む多岐の問題を解決しなければならない．これらの課題を解決するためには，医療の垣根を越えた，基礎物理分野などの他分野との共同研究が必要不可欠である．なお，本年度から国からの研究費補助を受け，4年半の研究開発期間で，新たなシステム開発を始めたところであり，その研究開発成果によって国内におけるがん治療全体の高水準化に繋げ，高精度のがん治療を多くの患者へ提供することを目指していこうと思う．

謝　辞

長年にわたり，本研究に御支援をしていただきました，元国立がん研究センターの江角浩安病院長(現東京理科大学生命医科学研究所)および荻野　尚部長(現メディポリスがん粒子線治療研究センター)，浜松ホトニクス株式会社電子管事業部電応システム部第13部門の岡本　俊様には大変深く感謝いたします．なお，本研究は，厚生労働科学研究費補助金(第3次対がん総合戦略研究事業及び医療技術実用化総合研究事業)の支援を受け実施された．

参考文献

1) Brahme A. Optimization of stationary and moving beam radiation therapy techniques. Radiother Oncol 1988; 12(2): 129-140.
2) Intensity Modulated Radiation Therapy Collaborative Working Group. Intensity-modulated radiotherapy: current status and issues of interest. Int J Radiat Oncol Biol Phys 2001; 51(4): 880-914.
3) http://ptcog.web.psi.ch/Archive/pat_statistics/Patientstatistics-updateMar2013.pdf
4) Simpson RG, Chen CT, Grubbs EA, et al. A 4-MV CT scanner for radiation therapy: the prototype system. Med Phys 1982; 9(4): 574-579.
5) ICRU Report 46, Photon, Electron, Proton and Neutron Interaction Date for Body Tissues 1992.
6) Nishio T, Ogino T, Shimbo M, et al. Distributions of β + decayed nucleus produced from the target fragment reaction in (CH2) n and patient liver targets by using a proton beam for therapy. Abstracts of the XXXIV PTCOG MEETING 2001; 15-16.
7) Nishio T, Sato T, Kitamura H, et al. Distributions of β+ decayed nuclei generated in the CH2 and H2O targets by the target nuclear fragment reaction using therapeutic MONO and SOBP proton beam. Med Phys 2005; 32: 1070-1082.
8) Nishio T, Miyatake A, Inoue K, et al. Experimental verification of proton beam monitoring in a human body by use of activity image of positron-emitting nuclei generated by nuclear fragmentation reaction. Radiol Phys Technol 2008; 1(1): 44-54.
9) Nishio T, Ogino T, Nomura K, et al. Dose-volume delivery guided proton therapy using beam on-line PET system. Med Phys 2006; 33(11): 4190-4197.
10) Nishio T, Miyatake A, Ogino T, et al. The development and clinical use of a Beam ON-LINE PET system mounted on a rotating gantry port in proton therapy. Int J Radiat Oncol Biol Phys 2010; 76(1): 277-286.
11) Miyatake A, Nishio T, Ogino T, et al. Measurement and verification of positron emitter nuclei generated at each treatment site by target nuclear fragment reactions in proton therapy. Med Phys 2010; 37(8): 4445-4455.
12) Miyatake A, Nishio T, Ogino T. Development of activity pencil beam algorithm using measured distribution data of positron emitter nuclei generated by proton irradiation of targets containing ^{12}C, ^{16}O and ^{40}Ca nuclei in preparation of clinical application. Med Phys 2011; 38(10): 5818-5829.
13) Miyatake A, Nishio T. Application of activity pencil beam algorithm using measured distribution data of positron emitter nuclei for therapeutic SOBP proton beam. Med Phys 2013; 40(9): 091709-1-9.

Application of activity pencil beam algorithm using measured distribution data of positron emitter nuclei for therapeutic SOBP proton beam

Aya Miyatake[a)]
Keen Medical Physics Co. Ltd., 901-4-4-4 Yushima, Bunkyo-ku, Tokyo 113-0034, Japan

Teiji Nishio
Particle Therapy Division, Research Center for Innovative Oncology, National Cancer Center, Kashiwa, 6-5-1 Kashiwano-ha, Kashiwa-shi, Chiba 277-8577, Japan

(Received 9 October 2012; revised 24 July 2013; accepted for publication 29 July 2013; published 16 August 2013)

Purpose: Recently, much research on imaging the clinical proton-irradiated volume using positron emitter nuclei based on target nuclear fragment reaction has been carried out. The purpose of this study is to develop an activity pencil beam (APB) algorithm for a simulation system for proton-activated positron-emitting imaging in clinical proton therapy using spread-out Bragg peak (SOBP) beams.

Methods: The target nuclei of activity distribution calculations are ^{12}C nuclei, ^{16}O nuclei, and ^{40}Ca nuclei, which are the main elements in a human body. Depth activity distributions with SOBP beam irradiations were obtained from the material information of ridge filter (RF) and depth activity distributions of compounds of the three target nuclei measured by BOLPs-RGp (beam ON-LINE PET system mounted on a rotating gantry port) with mono-energetic Bragg peak (MONO) beam irradiations. The calculated data of depth activity distributions with SOBP beam irradiations were sorted in terms of kind of nucleus, energy of proton beam, SOBP width, and thickness of fine degrader (FD), which were verified. The calculated depth activity distributions with SOBP beam irradiations were compared with the measured ones. APB kernels were made from the calculated depth activity distributions with SOBP beam irradiations to construct a simulation system using the APB algorithm for SOBP beams.

Results: The depth activity distributions were prepared using the material information of RF and the measured depth activity distributions with MONO beam irradiations for clinical therapy using SOBP beams. With the SOBP width widening, the distal fall-offs of depth activity distributions and the difference from the depth dose distributions were large. The shapes of the calculated depth activity distributions nearly agreed with those of the measured ones upon comparison between the two. The APB kernels of SOBP beams were prepared by making use of the data on depth activity distributions with SOBP beam irradiations that were made from the depth activity distributions with MONO beam irradiations and sorted in terms of energy, SOBP width, and thickness of FD. The data on APB kernels of SOBP beams were determined as installment data for the simulation system using the APB algorithm for SOBP beam irradiations.

Conclusions: A method of obtaining the depth activity distributions and the APB algorithm for clinical use of SOBP beams have been developed. It is suggested that the simulation system for imaging the clinical irradiated volume with the APB algorithm can be used in clinical proton therapy using SOBP beams by preparing and investigating the data on APB kernels of SOBP beams.
 [http://dx.doi.org/10.1118/1.4818057]

Key words: proton therapy, SOBP beam, imaging the clinical proton-irradiated volume, simulation of activity distribution, activity pencil beam algorithm, beam ON-LINE PET system, target nuclear fragment reaction

1. INTRODUCTION

Proton therapy is a form of radiotherapy that can be concentrated on a tumor using a scanned or modulated Bragg peak. To use this radiotherapy efficiently in a clinical context, it is necessary to evaluate the clinical proton-irradiated volume accurately. Therefore, proton therapy has been performed for patients with measurement using the Beam ON-LINE PET system mounted on a rotating gantry port (BOLPs-RGp) at the National Cancer Center, Kashiwa (NCCE), since October 2007 (Ref. 1). BOLPs-RGp was installed in a treatment room with the dual-ring double scattering method.[2,3] Some clinical analyses of clinical proton-irradiated volume were reported by verifying the patient data measured by BOLPs-RGp.[1,4]

Human body is mostly composed of five elements: H, C, N, O, and Ca. It is known that reaction cross section of $^{14}N(p, \alpha)^{11}$ C reaction is over 200 mb only around proton beam range (just before a beam stop)[5]. ^{11}C nuclei have a long half-life time of about 20 min. However, activity distributions are formed mainly by information of ^{15}O nuclei with short

half-life about 2 min because measurement time is several minutes at the most in a clinical case using online PET. In addition, compositional rate of N nuclei are smaller than H, C, O, and Ca nuclei in target organs for proton therapy (the rate of N: ~ 2.7%).[6] Therefore, it is thought that existence of N nuclei can be ignored in the clinical case using BOLPs-RGp. In case it needs time interval between the end of proton irradiation and the start of PET measurement such as offline PET, it may be necessary to consider existence of N nuclei because ^{11}C and ^{13}N (half-life about 10 min) with long half-life nuclei are main information for activity distributions. Consequently, important nuclei for imaging the clinical proton-irradiated volume in a patient's body are positron emitter nuclei of ^{11}C, ^{10}C, ^{15}O, ^{14}O, and ^{38}K, etc., generated by target nuclear fragment reaction of ^{12}C, ^{16}O, and ^{40}Ca nuclei with proton of therapeutic beam energy for proton therapy. A calculation algorithm, activity pencil beam (APB) algorithm, that has both sufficient accuracy and useful calculation time in clinical proton therapy for a simulation system of proton-activated positron-emitting imaging was developed and proposed.[7] The simulation system has some important functions: import function of CT image data, ROI information, a result data of calculated dose distributions in DICOM-RT Ion format and original formatted activity distribution data measured by BOLPs-RGp, calculation function of activity distributions using APB algorithm and verification function of comparison among calculated dose distributions, measured activity distributions and calculated activity distributions. For proton therapy with high accuracy, it is important to construct a simulation system for imaging the clinical proton-irradiated volume in clinical use. A lot of reports on phantom studies, simulation studies, patients studies and so on for proton therapy have been published.[1,4,7–21]

Some hospitals and facilities use pencil beam scanning for proton therapy and others use broad beam as spread-out Bragg peak (SOBP) beam. SOBP for the uniform dose distribution in the depth direction is the sum of several Bragg peaks made by a proton beam passing through bar-ridge filter (RF) or range modulators at staggered depths. In a facility using RF, a filter is designed in consideration of scattering and nuclear interaction effect within the filter itself to produce a three-dimensionally uniform SOBP.[22] In the simulation system discussed in our previous report, activity distribution is calculated using APB algorithm with APB kernels prepared by the data of mono-energetic (MONO) beam irradiations.[7] If an activity distribution with SOBP beam irradiation is calculated using the previous method, the required number of calculation sets is equal to the number of beams forming the SOBP. Furthermore, it needs enormous time to measure data for APB kernels that users should prepare for the simulation system using APB algorithm. These are reason for difficulty of the use of method reported in our previous report, because short calculation time and user-friendly system were required in a clinical radiotherapy context.

In our early publication, a calculated APB kernel for a MONO beam consists a magnitude based on measured positron-emitting activity along the depth and a Gaussian function for mimicking the effect of multiple Coulomb scattering.[5] The magnitude is characterized by the contributions of long and short half-life components. Based on calculated mono-energetic APB kernel without re-establishing parameters for the depth or lateral profile, a simple sum of contributions of each energy layer of mono-energetic protons for forming modulated proton (i.e., SOBP) can be performed.

In this paper, to make it possible to simulate an activity distribution with SOBP beam irradiation using APB algorithm, we establish making APB kernels with SOBP beam irradiation using measured depth activity distribution with MONO beam irradiation and the material information of RF. It becomes to propose an application of APB algorithm for proton therapy of SOBP beams.

2. MATERIALS AND METHODS

2.A. Clinical SOBP beam for proton therapy at NCCE

The dual-ring double scattering method has been used in the treatment room where BOLPs-RGp was installed at NCCE. After a proton beam passes through the dual-ring double scatters to produce a flat irradiation field in the lateral direction, it passes through an aluminum RF to produce a flat irradiation field in the depth direction.[3] RF prepared in our center allows us to select SOBP width from among eight grades between 30 and 100 mm in 10-mm steps.[3] Proton beam energies of 223, 179, and 138 MeV become those of 200, 159, and 121 MeV after a proton beam passes through the dual-ring double scatters. Proton ranges of 200, 159, and 121 MeV in the dual-ring double scattering system were shorter than those of 223, 179, and 138 MeV by 53.8, 39.6, and 27.7 mm, respectively.

Dose distributions were measured at intervals of 1 mm using a three-dimensional water phantom with a plane parallel ion chamber. The dose distributions at beam energies of 200, 159, and 121 MeV were measured with parameters of SOBP width and thickness of fine degrader (FD). FD is made of Lucite and used to adjust beam ranges. SOBP width was changed from 30 to 100 mm in 10-mm steps and the thickness of FD from 0 mm to the maximum thickness of 80 mm in the same steps. The maximum thickness of FD depends on beam energy and SOBP width. Percentage depth dose (PDD) was measured using the parallel ion chamber which was set at the position where isocenter was on the surface of the water. Distance from isocenter to FD is 989 mm and from isocenter to RF is 1696 mm. The water equivalent length of 1 cm FD (Lucite) is 1.16 cm by a preliminary experiment.

2.B. Calculation of depth activity distributions of clinical SOBP beam from measured depth activity distributions of MONO beam and material information of RF

SOBP is the sum of several beams (i beams) that a MONO beam is divided into by passing through RF. SOBP can be expressed using proton beam energy, material information of RF and the effect of multiple Coulomb scattering by RF and

FD such as the following Eq. (1),

$$\mathrm{SOBPd(E, RF, FD, z)} = \sum_{k}^{i}\{rf_k(\mathrm{E, RF}).fd_k(\mathrm{E, FD}) \cdot \mathrm{monod}_k(\mathrm{E, FD} = 0, \mathrm{z})\}. \quad (1)$$

Here, SOBPd denotes depth dose distribution with SOBP beam irradiation. SOBPd is a function with four parameters: incident proton energy, E, the information of RF and FD, RF and FD, and depth, z. Function of *rf* considers effect of energy loss, multiple Coulomb scattering and the number of protons caused by the information of RF. Function of *fd* also considers the scattering effect caused by thickness of FD. The monod denotes a depth-dose distribution measured in the case of MONO beam irradiation with incident proton energy E and FD = 0. You can replace depth-dose distribution with depth activity distribution with applying Eqs. (2) to (1),

$$\mathrm{SOBPd(E, RF, FD, z)} \rightarrow \mathrm{SOBPa(M, E, RF, FD, z)}$$
$$\mathrm{monod}_k(\mathrm{E, FD} = 0) \rightarrow \mathrm{monoa}_k(\mathrm{M, E, FD} = 0). \quad (2)$$

Here, SOBPa denotes depth activity distribution with SOBP beam irradiation. M denotes kind of target nucleus. The monoa denotes a depth activity distribution measured in the case of MONO beam irradiation. Depth activity distributions of SOBP beam (SOBP_act) can be calculated from measured depth activity distribution of MONO beam (MONO_act), material information of RF and FD thickness using Eqs. (1) and (2). In this study, the measured activity distributions of virtual positron emitter nuclei ($^{12}C_{virtual}$, $^{16}O_{virtual}$, and $^{40}C_{avirtual}$) reported in our previous study were used as the monoa (M = $^{12}C_{virtual}$, $^{16}O_{virtual}$, $^{40}Ca_{virtual}$; E = 121, 159, and 200 [MeV], FD = 0).[7] The virtual positron emitter nucleus was defined as the nuclei merged for various positron emitter nuclei generated from each target nucleus by target nuclear fragment reaction with proton beam irradiation.

Data of SOBP_act were prepared at three energies (121, 159, and 200 MeV), SOBP width for eight grades between 30 and 100 mm in 10-mm steps and the thickness of FD for nine levels between 0 and 80 mm in 10-mm steps.

2.C. Making of APB kernels for simulation of depth activity distributions using SOBP beam irradiations

If a calculation is performed using the method of simulation reported by Miyatake *et al.* (2011), it takes more time to calculate activity distributions with SOBP beam irradiations than MONO beam irradiations.[7] For example, to obtain a SOBP50 beam, a MONO beam is divided into 12 beams with different energies by passing through RF. Using the method reported by Miyatake *et al.* (2011) and the APB algorithm, SOBP_act is obtained by summing each calculated depth activity distribution made from 12 beams. Therefore, the calculation time required for simulating SOBP_act is 12 times that of MONO_act.

To shorten the calculation time, we propose a method which the APB kernels obtained by SOBP beam irradiations is prepared in advance. The APB algorithm which is a new method using APB kernels with SOBP beam irradiations can calculate SOBP_act with short time.

APB kernels were made from calculated SOBP_act based on measured MONO_act (see Sec. 2) and consideration of the effect of multiple Coulomb scattering, which was included in the lateral activity distributions with Gaussian form similar to proton dose calculation by pencil beam algorithm. The formula proposed by Lynch was used for the APB kernels in this study.[23] They were sorted by every clinical condition of SOBP beam (energy, SOBP width, and FD thickness).

3. RESULTS AND DISCUSSION

3.A. A Measured depth dose distributions of clinical SOBP beams at NCCE

Figure 1(a) is the measured depth dose distribution of each SOBP width at proton energy of 121, 159, and 200 MeV with FD = 0 mm. Figure 2(a) is the measured depth dose distribution of each FD thickness at proton energy of 121, 159, and 200 MeV with SOBP = 50 mm. All data of measured depth dose distributions of clinical SOBP beams were normalized at dose of SOBP center. The flatness of depth dose distribution in SOBP width was almost within ±1.5%. Dose at beam-entrance point in the SOBP width tends to fall by increase of FD thickness. It was observed that the measured beam ranges shifted regularly with a change of thickness of FD.

3.B. Comparison between calculated activity distributions and measured ones with SOBP beam irradiations

Figure 3 shows the calculated SOBP_act and the measured one around a range. The conditions of the irradiated proton beam were SOBP50-FD0 at 200 MeV. Comparing these distributions, an agreement within ±10% was observed. If we measure all of the data regarding SOBP_act to install a simulation system for imaging the clinical proton-irradiated volume, the measurement has to be carried out in each irradiation condition of three energies, eight SOBP widths and variable FD thickness. The total measurement time for all measurements is so enormous that preparation of all the data from the measurements is not feasible. Therefore, it was decided that the essential data to install the simulation system were to be obtained by calculating from the measured MONO_act and the material information of RF in our study.

3.C. Verification of the shape of calculated SOBP_act based on modulation of the measured MONO_act

Figures 1(b)–1(d) show measured MONO_act and the SOBP_act that were calculated from the MONO_act and the material information of RF. Activity distributions were normalized with each maximum value. Polyethylene, water, and calcium oxide were used as irradiation targets to measure activity distributions of positron emitter nuclei (^{11}C, ^{10}C, ^{15}O, ^{14}O, and ^{38}K, etc.) generated from three target nuclei (^{12}C, ^{16}O, and ^{40}Ca) in our previous study. Scaling factors

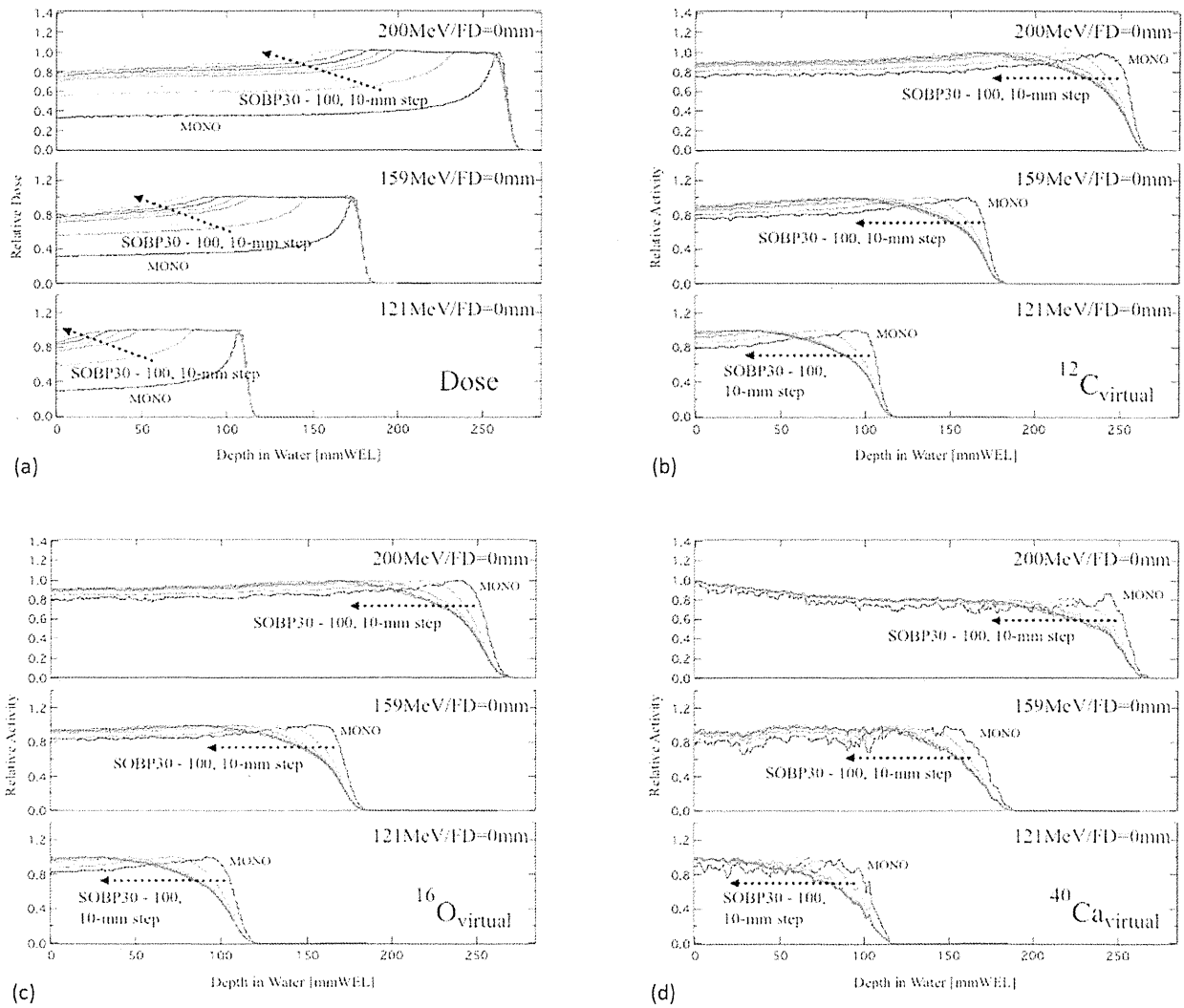

FIG. 1. (a) Measured depth dose distributions of MONO beams and SOBP beams, (b)–(d) Depth activity distributions of $^{12}C_{virtual}$, $^{16}O_{virtual}$, and $^{40}Ca_{virtual}$ in the case of SOBP beam irradiations. MONO activity distributions shown in (b)–(d) were measured. SOBP-depth activity distributions were calculated by modulation of measured MONO-depth activity distributions based on the material information of RF. The conditions of beam were FD = 0, SOBP widths from 30 to 100 mm with 10-mm steps at energies of 121, 159, and 200 MeV.

of polyethylene and calcium oxide against water calculated by measurement of beam range using proton beam.[7] It was observed that distal fall-off of the calculated SOBP_act and the differences in shapes between depth dose distributions and SOBP_act were wider with increasing SOBP width. The activity range (R_{act}), which is defined as a depth point whose relative activity value is 50%-value in SOBP-center normalized, was analyzed to verify a change of range position in SOBP_act and the result at 159 MeV is shown in Fig. 4. Although there were few changes in range positions in dose distributions with the parameter of SOBP width under constant FD thickness, R_{act} were shifted with SOBP width regularly in SOBP_act of $^{12}C_{virtual}$ and $^{16}O_{virtual}$. It is proved that ranges in SOBP_act were influenced by SOBP width and the kind of nucleus.

Calculated depth activity distributions of each kind of virtual nucleus with the parameter of FD thickness and constant SOBP50 and measured MONO_act are shown in Figs. 2(b)–2(d). Dose distributions almost kept their shapes and positions of ranges were shifted regularly with changes of FD thickness. In SOBP_act of three virtual nuclei, shapes changed more as FD thickness increased and ranges were shifted gradually with changes of FD thickness. It was found that shapes of SOBP_act were different for the three virtual nuclei and beam energies. Variations of R_{act} were analyzed about SOBP_act of each virtual nucleus with changing SOBP width and FD thickness. The result of analysis with a 159-MeV proton beam is shown in Fig. 5. It is illustrated that there was a linear relationship between range in SOBP_act and FD thickness within ±5% accuracy in each virtual nucleus regardless of changing SOBP width. Although the shapes of SOBP_act were influenced by FD thickness, the linear relationship was seen clearly. Therefore, we suppose that R_{act} can be estimated using the relationship with FD thickness. In addition, R_{act} can be

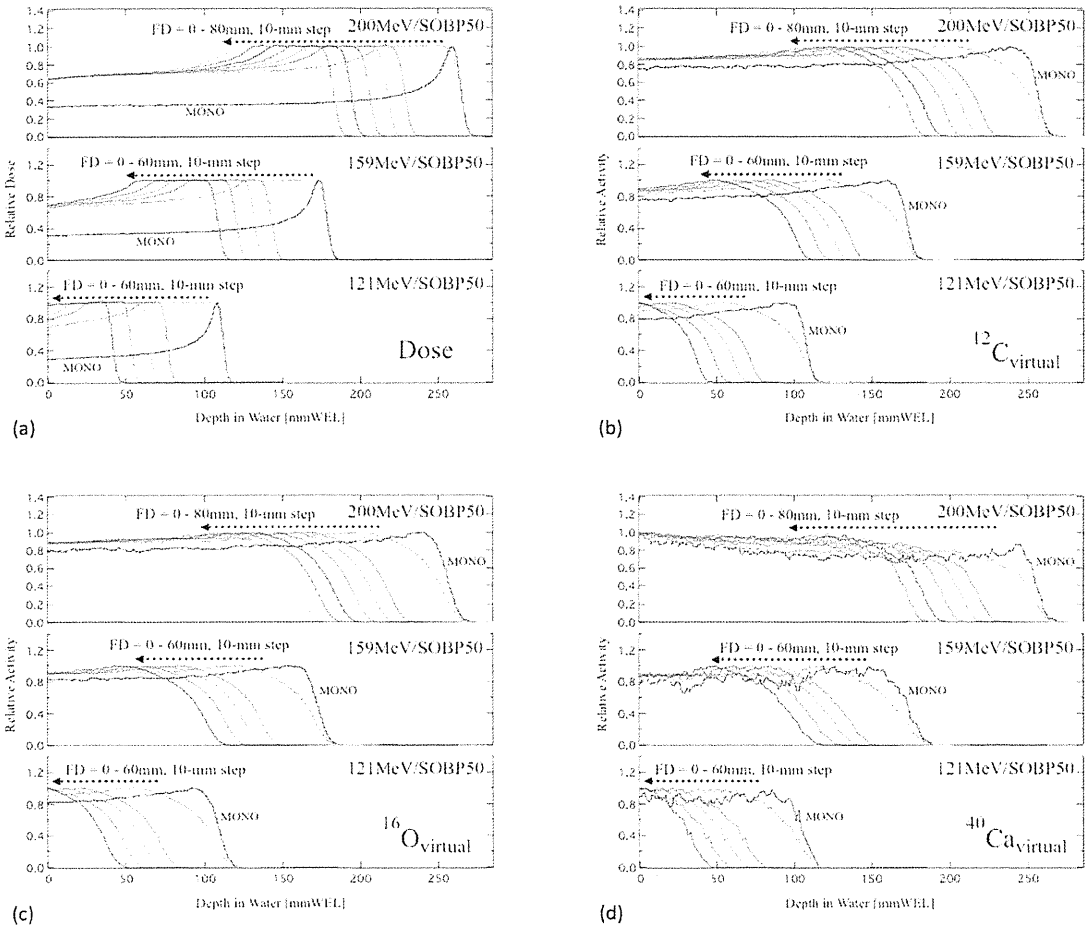

FIG. 2. (a) Measured depth dose distributions of MONO beams and SOBP beams, (b)–(d) Calculated depth activity distributions of $^{12}C_{virtual}$, $^{16}O_{virtual}$, and $^{40}Ca_{virtual}$ in the case of SOBP50 beam irradiations. MONO activity distributions shown in (b)–(d) were measured. SOBP-depth activity distributions were calculated by modulation of measured MONO-depth activity distributions based on the material information of RF. Proton beam energies were 121, 159, and 200 MeV. The thickness of FD was changed from 0 to 60 or 80 mm depending on beam energy.

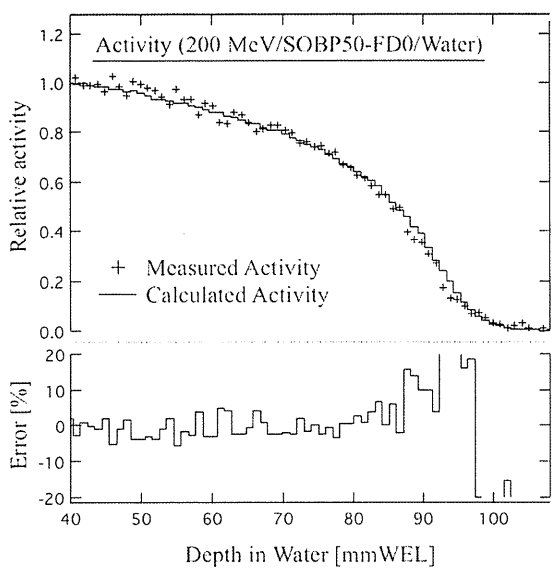

FIG. 3. Measured SOBP_act and calculated SOBP_act around a range with SOBP50-FD0 beam irradiation at 200 MeV in water. The shown error was calculated by defining the measured value as true.

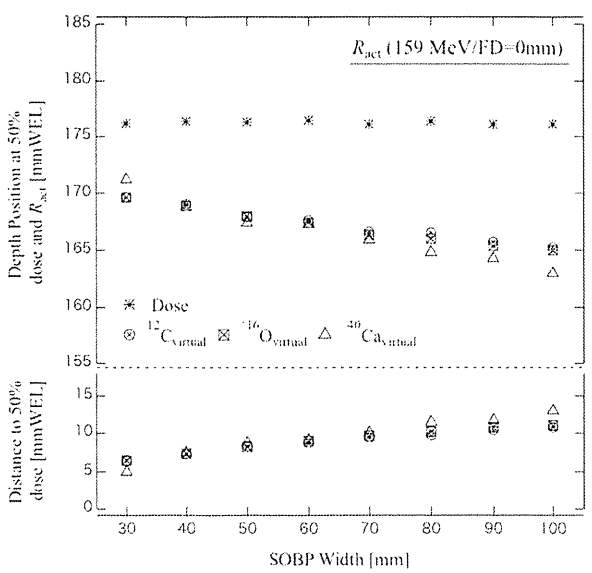

FIG. 4. Relationship between R_{act} and SOBP width in SOBP_act of each kind of virtual positron emitter nucleus in the beam irradiation condition of 159 MeV and FD = 0.

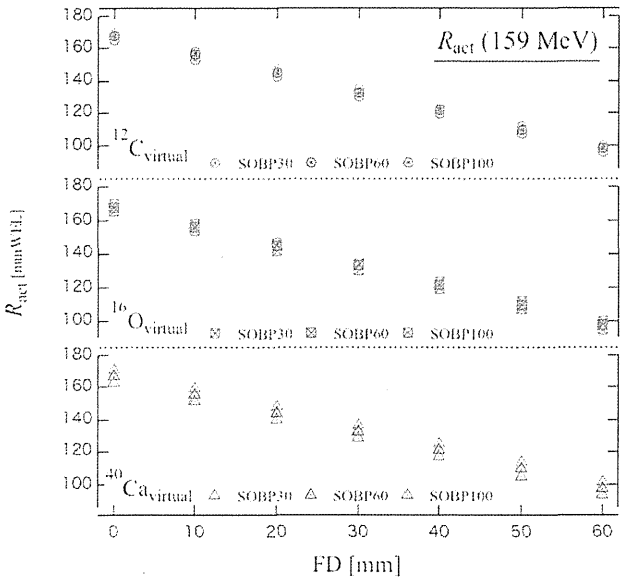

FIG. 5. Change of R_{act} with the parameter of FD thickness in SOBP_act of $^{12}C_{virtual}$, $^{16}O_{virtual}$, and $^{40}Ca_{virtual}$. The conditions of irradiated proton beam were SOBP30, SOBP60, and SOBP100 at 159 MeV.

expected to be an important parameter to estimate the range of dose distribution.

3.D. SOBP APB kernels for clinical proton therapy

APB kernels constructed by the calculated SOBP_act were prepared for simulation of imaging the clinical protonirradiated volume using the APB algorithm. The kernels of $^{12}C_{virtual}$, $^{16}O_{virtual}$, and $^{40}Ca_{virtual}$ were made in every irradiation condition of energy, SOBP width and FD thickness in our center. As an example of the kernels, depth or lateral activity (or dose) distributions and depth activity (or dose) distributions at a lateral point from the center axis by 1-mm steps are shown in Fig. 6. Dose distributions were measured and calculated in water.

3.E. Verification of a slope of SOBP between measured depth dose distributions and calculated activity distributions

SOBP has a slight slope of lower dose in the beam incident side with FD being thicker because the scatter of the

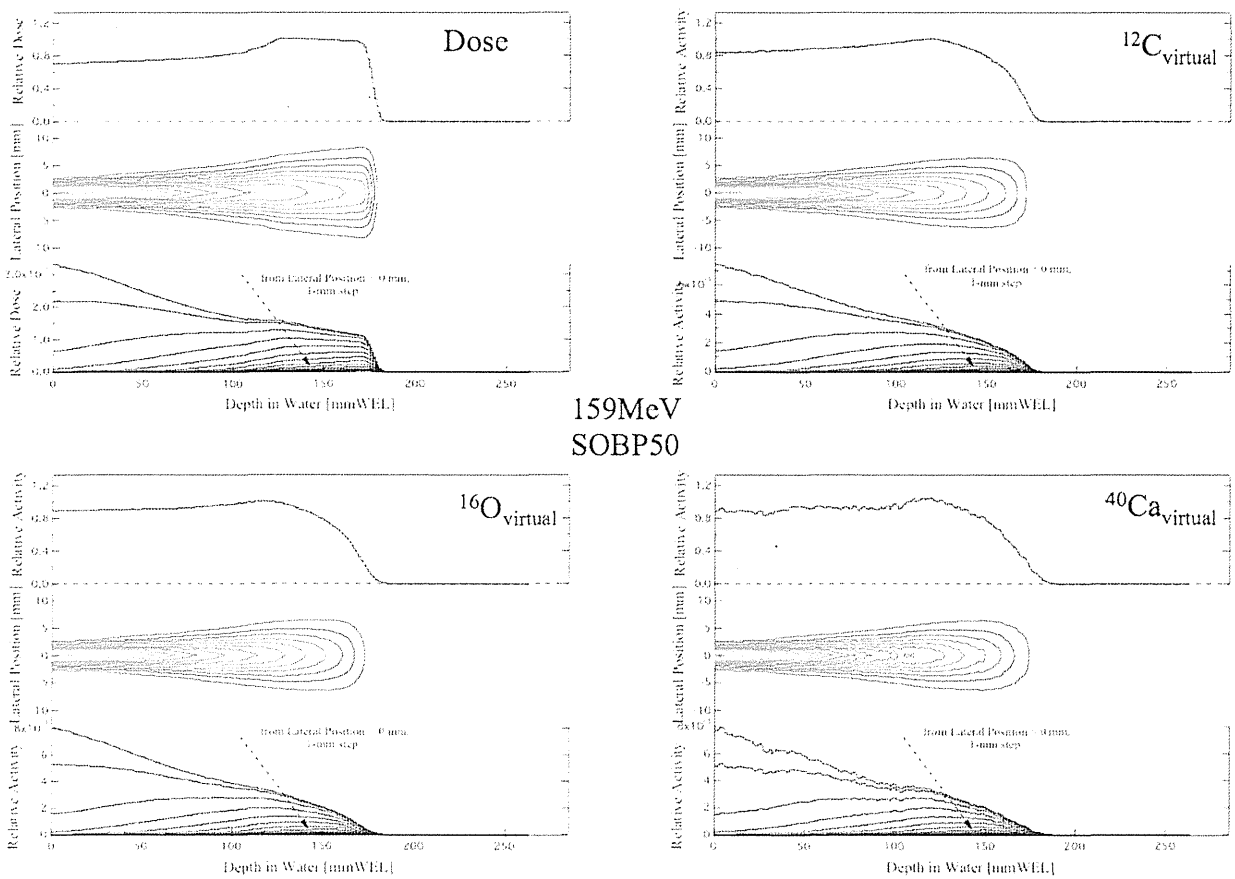

FIG. 6. The results of calculated dose and APB kernels of $^{12}C_{virtual}$, $^{16}O_{virtual}$, and $^{40}Ca_{virtual}$ with SOBP50-FD0-beam irradiation at 159 MeV. Each graph has three small graphs: (the upper) depth dose or activity distributions, (the middle) two-dimensional dose or APB kernels, and (the lower) depth dose or activity distributions toward the distance from the central proton beam axis.

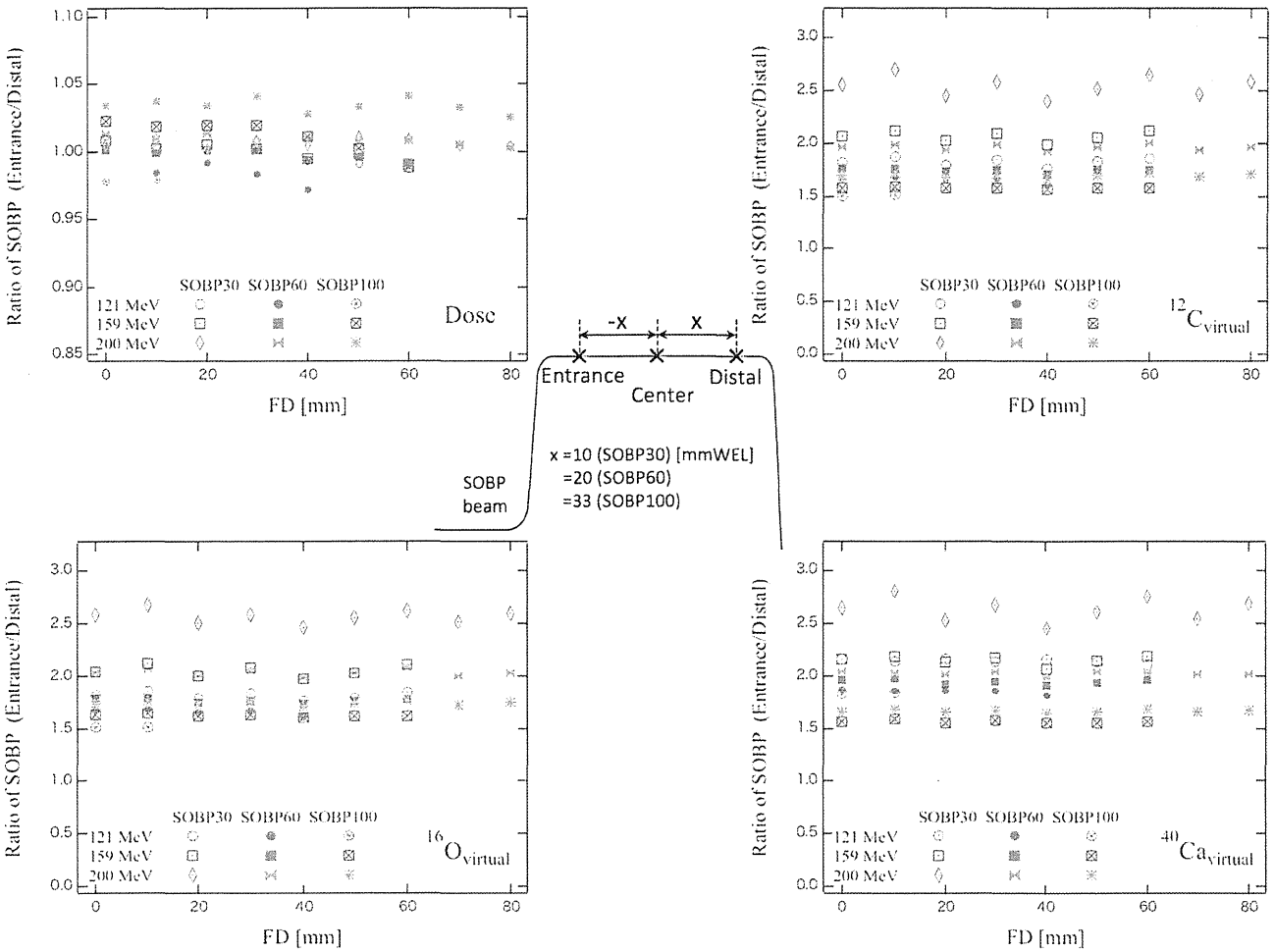

FIG. 7. Comparisons of dose distributions and SOBP_act of $^{12}C_{virtual}$, $^{16}O_{virtual}$, and $^{40}Ca_{virtual}$ in slopes of SOBP at three energies. An entrance was defined as the nearest point to an incident beam and a distal as the furthest point. The ratio of relative value (activity or dose) at the entrance to that at the distal was plotted with a parameter of FD thickness.

TABLE I. The degree of changes in SOBP's shape of SOBP_act toward that of dose distributions.

	R[a](activity distribution of virtual nucleus)/R[a](dose distribution)					
	SOBP30		SOBP60		SOBP100	
121 MeV	FD = 0	FD = 60	FD = 0	FD = 40	FD = 0	FD = 10
R($^{12}C_{virtual}$)/R(Dose)	1.8	1.9	1.7	1.7	1.5	1.5
R($^{16}O_{virtual}$)/R(Dose)	1.8	1.9	1.7	1.7	1.5	1.5
R($^{40}Ca_{virtual}$)/R(Dose)	2.1	2.1	1.9	1.9	1.9	1.9
159 MeV	FD = 0	FD = 60	FD = 0	FD = 60	FD = 0	FD = 60
R($^{12}C_{virtual}$)/R(Dose)	2.0	2.1	1.8	1.8	1.5	1.6
R($^{16}O_{virtual}$)/R(Dose)	2.0	2.1	1.8	1.8	1.6	1.6
R($^{40}Ca_{virtual}$)/R(Dose)	2.1	2.2	1.9	2.0	1.5	1.6
200 MeV	FD = 0	FD = 80	FD = 0	FD = 80	FD = 0	FD = 80
R($^{12}C_{virtual}$)/R(Dose)	2.5	2.6	1.9	1.9	1.6	1.7
R($^{16}O_{virtual}$)/R(Dose)	2.6	2.6	2.0	2.0	1.7	1.7
R($^{40}Ca_{virtual}$)/R(Dose)	2.6	2.7	2.0	2.0	1.6	1.6

[a]R: ratio of SOBP (entrance/distal).

beam through FD increases in the proton dose distribution. The change of slope of SOBP was verified every FD thickness in SOBP_act.

Values of relative activity or dose at verification points were analyzed in the dose distributions or calculated SOBP_act to verify changing slopes of SOBP. The verification points (entrance and distal) were set as ±10 mm WEL (SOBP30), ±20 mm WEL (SOBP60), and ±33 mm WEL (SOBP100) from a SOBP center point in a dose distribution under irradiation conditions of a certain energy, FD thickness, and SOBP width. Ratio between values at entrance and distal was calculated and Figure 7 shows the results of dose distributions and SOBP_act of three virtual nuclei at three energies. From this analysis, the lower the energy and the wider the SOBP width, the larger the degree of decline around beam entrance in SOBP became toward increasing of the FD thickness in dose distributions. In activity distributions, it was shown that the degree of each SOBP's slope was steeper than that in dose distributions.

The value was calculated from dividing the ratio of SOBP_act by that of dose distribution at each energy and SOBP width in order to clarify the change in SOBP's shape of SOBP_act toward that of the dose distribution. Table I shows these results of minimum and maximum FD thickness. The value of the ratio was about 2 to 3. In Table I, there were few changes of values with FD thickness increasing at one SOBP width and energy in every virtual nucleus. On the other hand, it was shown that the value of the ratio increased with narrower SOBP width and larger energy. Therefore, the coverage of irradiated volume in the activity distribution will become lower than that in the dose distribution around distal edge of SOBP. This tendency is more noticeable in narrower SOBP width and larger energy. And the predictive accuracy of the proton beam range in a patient will become low. It is very important for quality assurance of proton therapy to understand the differences between a dose distribution and an activity one.

4. CONCLUSIONS

A method to obtain SOBP_act using the measured MONO_act and material information of RF and the APB algorithm for SOBP beam irradiations were developed. It was proved that SOBP_act which is sorted in kind of nucleus, SOBP width, and thickness of FD could be reconstructed from measured MONO_act (with FD = 0) using the method within ±10% accuracy. Preparation of APB kernels of SOBP beams supports the use of a simulation system for imaging the clinical irradiated volume using the APB algorithm in clinical therapy with SOBP beams.

It was found that there were differences in the shapes of distributions in association with FD thickness and SOBP width between dose distributions and activity ones with SOBP beam irradiations. The possibility of estimating changes of ranges with FD thickness using a parameter of 50%-relative activity point (R_{act}) was suggested. The parameter (R_{act}) will be helpful to estimate the range of the beam in activity distributions resulting from a simulation using APB algorithm in the future.

Application of the simulation system to clinical proton therapy using SOBP beams is probably useful to provide treatments for patients with high accuracy. Comparison of the results of the measured data with those of the calculated data by the simulation system remains one of the important verifications to be carried out. The accuracy of calculation using the simulation system is under investigation. Our results in conjunction with *in vivo* dosimetry deserve further study.

ACKNOWLEDGMENTS

The authors would like to thank T. Okamoto of Hamamatsu Photonics K.K. for technical support. We also thank the staff members of the Proton Radiotherapy Department of the National Cancer Center, Kashiwa, for their help, and the members of SHI Accelerator Service Ltd. and Accelerator Engineering Inc. for the operation of the proton apparatus. This study was partially supported by grant-in-aid for Scientific Research (B) (23390308) and Health and Labor Sciences Research Grants (H22-Third Term Comprehensive Control Research for Cancer-025, H21-Clinical Research-006).

[a]Electronic mail: amiyatake@keenmp.co.jp

[1]T. Nishio, A. Miyatake, T. Ogino, K. Nakagawa, N. Saijo, and H. Esumi, "The development and clinical use of a beam ON-LINE PET system mounted on a rotating gantry port in proton therapy," Int. J. Radiat. Oncol., Biol., Phys. **76**, 277–286 (2010).

[2]T. Nishio, "Proton therapy facility at National Cancer Center, Kashiwa, Japan," J. At. Energy Soc. **41**, 1134–1138 (1999).

[3]T. Nishio, S. Kataoka, M. Tachibana, K. Matsumura, N. Uzawa, H. Saito, T. Sasano, M. Yamaguchi, and T. Ogino, "Development of a simple control system for uniform proton dose distribution in a dual-ring double scattering method," Phys. Med. Biol. **51**, 1249–1260 (2006).

[4]A. Miyatake, T. Nishio, T. Ogino, N. Saijo, H. Esumi, and M. Uesaka, "Measurement and verification of positron emitter nuclei generated at each treatment site by target nuclear fragment reactions in proton therapy," Med. Phys. **37**(8), 4445–4455 (2010).

[5]See http://www.nndc.bnl.gov/ for NNDC.

[6]ICRU, "Photon, electron, proton and neutron interaction date for body tissues," ICRU Report No. 46 (ICRU Publications, Washington, DC, 1992), pp. 11–13.

[7]A. Miyatake, T. Nishio, and T. Ogino, "Development of activity pencil beam algorithm using measured distribution data of positron emitter nuclei generated by proton irradiation of targets containing ^{12}C, ^{16}O, and ^{40}Ca nuclei in preparation of clinical application," Med. Phys. **38**(10), 5818–5829 (2011).

[8]G. W. Bennett, A. C. Goldberg, G. S. Levine, J. Guthy, and J. Balsamo, "Beam localization via 15O activation in proton-radiation therapy," Nucl. Instrum. Methods **125**, 333–338 (1975).

[9]U. Oelfke, G. Lam, and M. Atkins, "Proton dose monitoring with PET: Quantitative studies in Lucite," Phys. Med. Biol. **41**, 177–196 (1996).

[10]D. W. Litzenberg, D. A. Roberts, M. Y. Lee, K. Pham, A. M. Vander Molen, R. Ronningen, and F. D. Becchetti, "On-line monitoring of radiotherapy beams: Experimental results with proton beams," Med. Phys. **26**(6), 992–1006 (1999).

[11]K. Parodi, and W. Enghardt, "Potential application of PET in quality assurance of proton therapy," Phys. Med. Biol. **45**, N151–N156 (2000).

[12]T. Nishio, T. Ogino, M. Shimbo, S. Katsuta, S. Kawasaki, T. Murakami, T. Sato, Y. Kojima, K. Murakami, and H. Ikeda, "Distributions of β^+ decayed nucleus produced from the target fragment reaction in $(CH_2)n$ and patient liver targets by using a proton beam for therapy," Abstracts of the XXXIV PTCOG Meeting, Boston, MA (2001), pp. 15–16.

[13]K. Parodi, W. Enghardt, and T. Haberer, "In-beam PET measurements of β^+ radioactivity induced by proton beams," Phys. Med. Biol. **47**, 21–36 (2002).
[14]Y. Hishikawa, K. Kagawa, M. Murakami, H. Sasaki, T. Akagi, and M. Abe, "Usefulness of positron-emission tomographic images after proton therapy," Int. J. Radiat. Oncol., Biol., Phys. **53**, 1388–1391 (2002).
[15]T. Nishio, T. Sato, H. Kitamura, K. Murakami, and T. Ogino, "Distributions of β^+ decayed nuclei generated in the CH_2 and H_2O targets by the target nuclear fragment reaction using therapeutic MONO and SOBP proton beam," Med. Phys. **32**(4), 1070–1082 (2005).
[16]K. Parodi, F. Ponisch, and W. Enghardt, "Experimental study on the feasibility of in-beam PET for accurate monitoring of proton therapy," IEEE Trans. Nucl. Sci. **52**, 778–786 (2005).
[17]T. Nishio, T. Ogino, K. Nomura, and H. Uchida, "Dose-volume delivery guided proton therapy using beam ON-LINE PET system," Med. Phys. **33**(11), 4190–4197 (2006).
[18]K. Parodi, H. Paganetti, E. Cascio, J. B. Flanz, A. A. Bonab, N. M. Alpert, K. Lohmann, and T. Bortfeld, "PET/CT imaging for treatment verification after proton therapy: A study with plastic phantoms and metallic implants," Med. Phys. **34**(2), 419–435 (2007).
[19]K. Parodi, A. Ferrari, F. Sommerer, and H. Paganetti, "Clinical CT-based calculations of dose and positron emitter distributions in proton therapy using the FLUKA Monte Carlo code," Phys. Med. Biol. **52**, 3369–3387 (2007).
[20]K. Parodi, H. Paganetti, H. A. Shih, S. Michaud, J. S. Loeffler, T. F. Delaney, N. J. Liebsch, J. E. Munzenrider, A. J. Fischman, A. Knopf, and T. Bortfeld, "Patient study of in vivo verification of beam delivery and range, using positron emission tomography and computed tomography imaging after proton therapy," Int. J. Radiat. Oncol., Biol., Phys. **68**(3), 920–934 (2007).
[21]T. Nishio, A. Miyatake, K. Inoue, S. Katsuta, T. Gomi-Miyagishi, R. Kohno, S. Kameoka, K. Nakagawa, and T. Ogino, "Experimental verification of proton beam monitoring in a human body by use of activity image of positron-emitting nuclei generated by nuclear fragmentation reaction," Radiol. Phys. Technol. **1**(1), 44–54 (2008).
[22]T. Akagi, A. Higashi, H. Tsugami, H. Sakamoto, Y. Masuda, and Y. Hishikawa, "Ridge filter design for proton therapy at Hyogo Ion Beam Medical Center," Phys. Med. Biol. **48**, N301–N312 (2003).
[23]R. G. Lynch, and I. O. Dahl, "Approximations to multiple Coulomb scattering," Nucl. Instrum. Methods Phys. Res. B **58**, 6–10 (1991).

IOP PUBLISHING PHYSICS IN MEDICINE AND BIOLOGY

Phys. Med. Biol. **58** (2013) 1169–1184 doi:10.1088/0031-9155/58/4/1169

Application of the pencil-beam redefinition algorithm in heterogeneous media for proton beam therapy

Y Egashira[1], T Nishio[2], K Hotta[2], R Kohno[2] and M Uesaka[1]

[1] Department of Bioengineering, Graduate School of Engineering, University of Tokyo, 2-11-16, Yayoi, Bunkyo-ku, Tokyo 113-8656, Japan
[2] Particle Therapy Division, Research Centre for Innovative Oncology, National Cancer Centre, Kashiwa, 6-5-1 Kashiwanoha, Kashiwa-shi, Chiba 277-8577, Japan

E-mail: y.egashir@gmail.com

Received 10 October 2012, in final form 6 December 2012
Published 31 January 2013
Online at stacks.iop.org/PMB/58/1169

Abstract

In proton beam therapy, changes in the proton range due to lateral heterogeneity may cause serious errors in the dose distribution. In the present study, the pencil-beam redefinition algorithm (PBRA) was applied to proton beam therapy to address the problem of lateral density heterogeneity. In the calculation, the phase-space parameters were characterized for multiple range (i.e. proton energy) bins for given pencil beams. The particles that were included in each pencil beam were transported and redefined periodically until they had stopped. The redefined beams formed a detouring path that was different from that of the non-redefined pencil beams, and the path of each redefined beam was straight. The results calculated by the PBRA were compared with measured proton dose distributions in a heterogeneous slab phantom and an anthropomorphic phantom. Through the beam redefinition process, the PBRA was able to predict the measured proton-detouring effects. Therefore, the PBRA may allow improved calculation accuracy when dealing with lateral heterogeneities in proton therapy applications.

(Some figures may appear in colour only in the online journal)

1. Introduction

Pencil-beam (PB) algorithms (PBAs) (Hogstrom *et al* 1981, Petti 1992, Russell *et al* 1995, Hong *et al* 1996, Schaffner *et al* 1999, Russell *et al* 2000, Szymanowski *et al* 2001, Szymanoqski and Oelfke 2002) are among the most widely used models in the treatment planning of radiation therapy using charged particles (i.e. electron, proton, carbon ion, etc). In a homogeneous material, the accuracy of the PBA is satisfactory within a reasonable computing time. In a heterogeneous media, however, PBA calculations extremely limit its accuracy because of the central-axis approximation. Some particles included in such PBs may

extend beyond the interface of the density heterogeneity. Several techniques for addressing the problem of lateral density heterogeneities have been introduced into the PBAs. Schaffner *et al* (1999) reduced the overreaching of protons by splitting each scanning beam into small virtual pencil beams for dose calculation on the patient surface. The central-axis semiinfinite slab approximation proposed by Szymanoqski and Oelfke (2002) introduced a supplementary scaling acting on the PB off-axis distribution. This two-dimensional density scaling of the PB calculation has also improved the calculation accuracy around lateral density heterogeneities.

For electron therapy, Shiu and Hogstrom (1991) proposed the PB redefinition algorithm (PBRA) to overcome the limitations of the semifinite slab approximation inherent in conventional PBA calculations. Boyd *et al* (2001) reported that the PBRA improved the electron dose calculation for heterogeneities in cases of simple phantom geometries. For beam transportation in the Fermi–Eyges theory (Eyges 1948), three physical quantities of the particles are used: the spatial variance $\overline{t^2}$, angular variance $\overline{\theta^2}$, and angular-spatial covariance $\overline{\theta t}$ (Hollmark *et al* 2004, Kanematsu *et al* 2008). The PBRA handles the particle flow and energy at each redefinition plane. The physical quantities are characterized for multiple energy bins for a given PB. A concept similar to the PBRA was applied to heavy particles for computational modelling of beam-customization devices such as collimators and a range compensator, in which particle flow in the transverse plane was considered in the absence of heterogeneity (Kanematsu *et al* 2008). Without residual range variation, in such geometry, the particles could not be distinguished from the PBs in terms of statistical parameters such as phase space parameters and number of particles. Modulated range loss and scattering effects from the range and human body prevented the application of the redefinition technique, due to the range variation of the PBs. Therefore, to improve the calculation accuracy of the redefinition technique, the particle flow in energy space should be considered.

We previously proposed the spatial resampling technique (SRPBA), which was a special case of the PBRA with one-dimensional (1D) density scaling and a limited number of redefinition planes (up to two) (Egashira *et al* 2012). This method improved the calculation accuracy of the proton dose distribution in simple geometries. However, proton energy degrades and scatters further out after beam redefinition, and such broadened PBs may overreach lateral borders of heterogeneities. Therefore, the depth of the second redefinition plane strongly affected its accuracy and performance. Moreover, some correlation factors were required to calculate the angular distribution of the particles included in the redefined PB, due to the use of 1D density scaling.

Protons, like electrons, gradually lose energy in a material because of their Coulomb collisions with atoms. Their rate of energy loss increases as their energy decreases. Protons have a Bragg peak in the human body, in which their scattering angle is smaller than that of electrons. In particular, in a passive scattering method, a patient-specific range compensator should be attached at the nozzle exit to achieve conformity of the proton dose. Protons drift between the range compensator and patient body, forming a complicated energy spectrum at the patient surface. The resultant dose is severely affected by the particle path until the particles are stopped. In the PBRA, the PB parameters are characterized for proton energy (i.e. residual range) bins for the given PBs. Particles in each PB are transported and redefined periodically until all of the protons are stopped. Beam transport based on the Fermi–Eyges theory may allow the interval between the redefinition planes to be determined arbitrarily without any correlation factors. The PBRA effectively restricts the size of the PBs and considers the irregular paths of protons along the human body, thereby addressing the problem of lateral density heterogeneity.

In addition to the accuracy, the computational time of the treatment planning system is also an important factor. Intrinsically, the PBRA is computationally demanding because it utilizes

multiple energy bins for PB transport and dose deposition. Whereas the SRPBA regulates the number of redefinition planes for fast computation, the use of multiple energy bins of the PBs in the PBRA may improve the accuracy. For clinical use, the PBRA for proton beam therapy should be implemented within a reasonable computation time.

The purpose of this study was to evaluate the PBRA with respect to managing lateral density heterogeneity, by performing measurements in a heterogeneous slab phantom and an anthropomorphic phantom for proton therapy. Additionally, a GPU-based calculation was applied to accelerate the performance of the PBRA for proton therapy.

2. Materials and methods

2.1. Proton PBRA

In this section, we briefly describe the PBRA that was originally proposed by Shiu and Hogstrom (1991). In the PBRA calculation for proton therapy, PBs are generated at the entrance to the range compensator. Subsequently, beam transport, beam redefinition, and dose deposition are periodically repeated until all of the particles that are included in the beam are stopped in the patient. In the calculations, the height of the isocentre is set to $z = 0$. Other coordinate systems are shown in figures 3 and 4.

2.1.1. Beam generation. Analogous to the PBA (Hong *et al* 1996, Szymanowski *et al* 2001), the effective source of the PBRA is approximated as a Gaussian, with a standard deviation of σ_{src} at a height $z = z_{\mathrm{src}}$. The mean direction of the protons for each PB, with slopes a_x and a_y, defines the fan lines from the effective source. Parameters that are related to the PB generation (Kanematsu *et al* 2008) are defined at the entrance to the range compensator at $z = z_c$, as follows:

$$x_{\mathrm{axis}\,ij} = x_j(z_c),\ y_{\mathrm{axis}\,ij} = y_i(z_c) \tag{1}$$

$$a_x(z_c)_{ij} = \frac{x_j(z_c)}{|z_c - z_{\mathrm{src}}|},\ a_y(z_c)_{ij} = \frac{y_i(z_c)}{|z_c - z_{\mathrm{src}}|} \tag{2}$$

$$\overline{\theta^2}_{ij}(z_c) = \frac{\sigma^2_{\mathrm{src}}}{(z_c - z_{\mathrm{src}})^2},\ \overline{\theta t}_{ij}(z_c) = \frac{\delta^2_{xy}}{12|z_c - z_{src}|},\ \overline{t^2}_{ij}(z_c) = \frac{\delta^2_{xy}}{12} \tag{3}$$

where $x_{\mathrm{axis}\,ij}$ and $y_{\mathrm{axis}\,ij}$ are the central axis positions of the PB_{ij} in x and y, respectively; and δ_{xy} is the calculation grid size. $R(z_c)$ is defined as the residual range at $z = z_c$. Inside the range compensator, the PBs are scattered from the effective scattering origin of the range compensator (Gottschalk *et al* 1993) and consecutively transported to the next plane.

2.1.2. Beam transport. During the transport of PBs in a material of interval Δz, parameter increments (Kanematsu 2009a) are calculated as follows:

$$\Delta x_{\mathrm{axis}\,ij} = a_{x\,ij}\Delta z,\ \Delta y_{\mathrm{axis}\,ij} = a_{y\,ij}\Delta z,\ \Delta s = \sqrt{a^2_{x\,ij} + a^2_{y\,ij} + 1}\cdot\Delta z \tag{4}$$

$$\Delta R = -WEL(\Delta s) \tag{5}$$

$$\Delta\overline{\theta^2} = 0.001\cdot\ln\frac{R}{R+\Delta R},\ \Delta\overline{\theta t} = \left(\overline{\theta^2} + \frac{1}{2}\Delta\overline{\theta^2}\right)\cdot\Delta s,$$
$$\Delta\overline{t^2} = \left[2\overline{\theta t} + \left(\overline{\theta^2} + \frac{1}{3}\Delta\overline{\theta^2}\right)\Delta s\right]\Delta s \tag{6}$$

where the water equivalent length of Δs ($WEL(\Delta s)$) corresponds to the range loss in the beam path Δs.

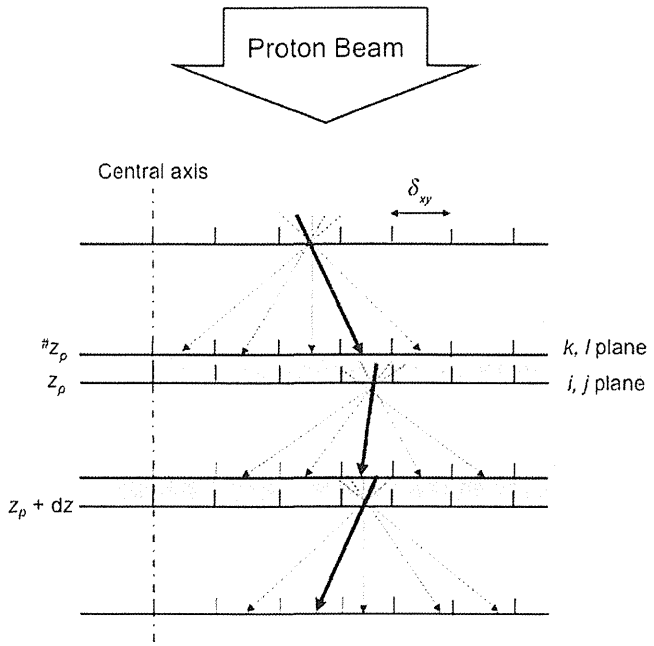

Figure 1. Illustration of the redefinition procedure: pencil beams are redefined at each depth, where the phase-space parameters should be recalculated.

2.1.3. Beam redefinition. The PB parameters need to be characterized for multiple energy (i.e. residual range) bins in a material. Figure 1 illustrate the beam redefinition in the patient plane $z = z_p$.

The plane $z = {}^{\#}z_p$ (i.e. k, l plane) is defined immediately upstream of the plane $z = z_p$ (i.e. i, j plane), where the PBs have not been redefined. In the PBRA calculation at $z = z_p$, the increment of the particles included in pixel (i, j, z_p) for the mth range (i.e. energy) bin $\left(\Delta N^{\#}_{k,l}\right)_m$ is defined as the contribution of particle numbers in pixel (i, j, z_p) from the pixel (k, l, $^{\#}z_p$) and is described as follows:

$$(\Delta N^{\#}_{k,l})_m = \sum_{\substack{n=1 \\ \in R_m \leqslant (\overline{R}^{\#}_{kl})_n < R_{m+1}}}^{R_b} (N^{\#}_{kl})_n \cdot \frac{1}{2}\left[\operatorname{erf}\left(\frac{(\Delta x^{\#})_n + \frac{\delta_{xy}}{2}}{\sqrt{2\left(\overline{t^2}^{\#}_{kl}\right)_n}}\right) - \operatorname{erf}\left(\frac{(\Delta x^{\#})_n - \frac{\delta_{xy}}{2}}{\sqrt{2\left(\overline{t^2}^{\#}_{kl}\right)_n}}\right)\right] \times \frac{1}{2}\left[\operatorname{erf}\left(\frac{(\Delta y^{\#})_n + \frac{\delta_{xy}}{2}}{\sqrt{2\left(\overline{t^2}^{\#}_{kl}\right)_n}}\right) - \operatorname{erf}\left(\frac{(\Delta y^{\#})_n - \frac{\delta_{xy}}{2}}{\sqrt{2\left(\overline{t^2}^{\#}_{kl}\right)_n}}\right)\right] \tag{7}$$

where $(N^{\#}_{kl})_n$ is the number of particles included in pixel (k, l, $^{\#}z_p$) for the nth range bin; R_b is the number of range bins; and $(\overline{R}^{\#}_{kl})_n$ is the residual range of protons falling in the mth range bin, which satisfies $R_m \leqslant (\overline{R}^{\#}_{kl})_n < R_{m+1}$. $(\Delta x^{\#})_n$ and $(\Delta y^{\#})_n$ are the distance between the central axis position of the PB and the calculation grid.

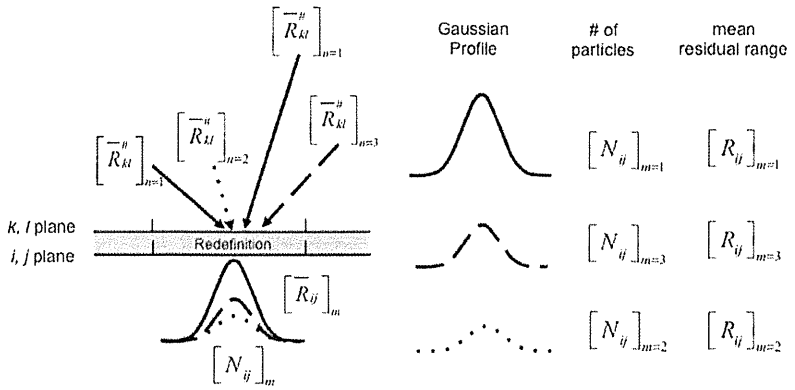

Figure 2. Illustration of the beam generation immediately after redefinition: Pencil beams with the residual range $(\overline{R}^{\#}_{kl})_n$ are transported to a calculation grid. The length of each arrow represents the number of particles. After redefinition, 'm' pencil beams are generated from the calculation grid. Area under the Gaussian profile represents the number of particles for the mth range bin $[N_{ij}]_m$. $[N_{ij}]_m$ and the mean residual range of the particles $[R_{ij}]_m$ in the patient plane $z = z_p$ are given in (8) and (9).

The number of particles for the mth range bin can be determined by summing the contribution from all of the range bins of the other pixels, as follows:

$$[N_{ij}(z_p)]_m = \sum_{k,l} [\Delta N^{\#}_{kl}]_m. \tag{8}$$

The mean residual range of the particles $[N_{ij}]_m$ in pixel (i, j, z_p) for the mth range bins is given by:

$$\begin{aligned}[\overline{R_{ij}}(z_p)]_m = \frac{1}{[N_{ij}(z_p)]_m} \sum_{k,l} \sum_{\substack{n=1 \\ \in R_m \leqslant (\overline{R}^{\#}_{kl})_n < R_{m+1}}}^{R_b} & (\overline{R}^{\#}_{kl})_n \cdot (N^{\#}_{kl})_n \\ \times \frac{1}{2} \left[\operatorname{erf}\left(\frac{(\Delta x^{\#})_n + \frac{\delta_{xy}}{2}}{\sqrt{2(\overline{t^2}^{\#}_{kl})_n}} \right) - \operatorname{erf}\left(\frac{(\Delta x^{\#})_n - \frac{\delta_{xy}}{2}}{\sqrt{2(\overline{t^2}^{\#}_{kl})_n}} \right) \right] & \\ \times \frac{1}{2} \left[\operatorname{erf}\left(\frac{(\Delta y^{\#})_n + \frac{\delta_{xy}}{2}}{\sqrt{2(\overline{t^2}^{\#}_{kl})_n}} \right) - \operatorname{erf}\left(\frac{(\Delta y^{\#})_n - \frac{\delta_{xy}}{2}}{\sqrt{2(\overline{t^2}^{\#}_{kl})_n}} \right) \right]. \end{aligned} \tag{9}$$

As a result of the redefinition, the mth PBs (the total number of which is represented by R_b) are generated from pixel (i, j, z_p) (see figure 2).

As described in the appendix, other statistical and phase-space parameters of the redefined beam on the z_p plane for the mth range bin may be calculated in the same manner, by using the equations defined by Kanematsu *et al* (2008).

2.1.4. Dose deposition. The total dose distribution $D(x, y)$ at a given depth in the patient is given as follows:

$$D(x, y) = \sum_{i,j} \sum_{m=1}^{R_b} \frac{(N_{ij})_m (C_{ij})_m}{2\pi \left(\overline{t^2}_{ij}\right)_m} \exp\left(-\frac{(\Delta x)^2_m + (\Delta y)^2_m}{2\left(\overline{t^2}_{ij}\right)_m} \right) \tag{10}$$